Journal Pre-proof

Polymer-cement composites with adhesion and re-adhesion (healing) to casing capability for geothermal wellbore applications

Kenton A. Rod, Carlos A. Fernandez, Manh-Thuong Nguyen, James B. Gardiner, Nicolas J. Huerta, Vassiliki-Alexandra Glezakou, Tamas Varga, Roger Rousseau, Phillip K. Koech

PII: S0958-9465(19)31333-2

DOI: https://doi.org/10.1016/j.cemconcomp.2019.103490

Reference: CECO 103490

To appear in: *Cement and Concrete Composites*

Received Date: 10 April 2019

Revised Date: 21 November 2019

Accepted Date: 16 December 2019

Please cite this article as: K.A. Rod, C.A. Fernandez, M.-T. Nguyen, J.B. Gardiner, N.J. Huerta, V.-A. Glezakou, T. Varga, R. Rousseau, P.K. Koech, Polymer-cement composites with adhesion and re-adhesion (healing) to casing capability for geothermal wellbore applications, *Cement and Concrete Composites*, https://doi.org/10.1016/j.cemconcomp.2019.103490.

Polymer-cement composites with adhesion and re-adhesion (healing) to casing capability for geothermal wellbore applications

Kenton A. Rod[1#], Carlos A. Fernandez[1 # +], Manh-Thuong Nguyen[2], James B. Gardiner, Nicolas J. Huerta[4], Vassiliki-Alexandra Glezakou[2], Tamas Varga[5], Roger Rousseau[2], Phillip K. Koech[1]

[1]Energy and Environment Directorate, Pacific Northwest National Laboratory, Richland WA

[2]Physical and Computational Sciences Directorate, Pacific Northwest National Laboratory, Richland WA

[3]National Environmental Technology Laboratory, Pittsburgh, PA

[4]National Environmental Technology Laboratory, Albany, OR

[5]Environmental and Molecular Sciences Laboratory, Pacific Northwest National Laboratory, Richland, WA

# Kenton A. Rod and Carlos A. Fernandez contributed equally to this manuscript

+ Carlos.Fernandez@pnnl.gov

ABSTRACT

Deterioration of cement/casing adhesion in wellbore scenarios can result in unwanted and potentially harmful leakage with the potential of serious repair costs. In this work, the authors explore the use of self-healing polymers added to conventional wellbore cements as a way to bring about self-healing and readhering (to casing) properties to the composite. Self-healing capability was demonstrated by permeability analysis showing that polymer-cement composites reduce flow by 50-70% at cement bulk and at the cement/steel interface. Use of atomistic simulations imply that these polymers have good wetting properties on the steel surfaces. Interactions between steel/polymer and cement/polymer are complementary, resulting in a wider range of bonding patterns. Cracks seem to expose under-coordinated sites that result in more bonding interactions, which agrees well with the permeability measurements showing high degree of healed cracks and cement-steel interfacial gaps together with an overall increased in structural integrity of these advanced polymer-cement composite materials.

Key words: cement-casing; bond strength; polymers; composite; oil well cement; geothermal

1 Introduction

Wellbore integrity is a significant environmental consideration in industries which use deep production wells such as in geothermal energy production. During wellbore construction, cement and cement composites are injected into the annulus between the geologic formation and the wellbore casing to hydraulically isolate production zones from overlying aquifers[1]. When applied using strict industry standards, cement and cement composites can extend the life of a producing well as well as protect the near surface environment. The potential for short life of wells and expensive remediation costs can hinder the development of geothermal energy despite of the fact that a large number of reserves of this clean energy alternative exist in the United States and around the globe[2]. A study of over 380,000 wells worldwide found that nearly 7% of wells experience wellbore failure[3] with one of the main reasons being the high temperature (up to 400 °C), thermal cycles, and chemically corrosive (typically hypersaline, CO_2 and H_2S rich) environments[4] typical of low and high temperature geothermal systems. Failure of the wellbore cement can be due to a combination of chemical degradation, fracturing, and deboning from the host rock or well casing.

Wellbore integrity issues are most common in the form of leakage pathways allowing for unwanted fluid migration. Cement bonding to the interface of both the casing and host rock has been identified as one of the most significant wellbore integrity issues[5]. This can be the result of extreme chemical and physical conditions of geothermal and oil and gas environments. With exposure to typical hypersaline, CO_2 and H_2S rich environments significant corrosion of the steel casing can occur[6]. This corrosion has been demonstrated to escalate by the high temperatures and by high chloride concentration of natural brine water and from drilling fluids[4]. Extreme temperatures and temperature variations due to the injection of cool fluids into the high

temperature subsurface (thermal shock) can induce debonding of cement to casing[4]. Portland cement has a low bond strength with steel which can debond due to thermal shock resulting in fluid migration pathways[7], and in a reduced pressure required to induce fractures[8]. Thermal shock has been found to reduce bond strength up to 69% for cement to casing[9].

To improve wellbore cement integrity the authors have developed a self-healing polymer-cement composite (composite 1) to be used in geothermal wellbore applications at different temperatures. Composite 1, which consist in a mixture of cement H and silica flour with 10 wt% of a crosslinked thermoset epoxy resin, was developed for temperatures of up to 200 °C and recently reported to have self-healing capability for fractures and openings in the cement matrix[10, 11]. The thermoset resin is crosslinked with pentaerythritol tetrakis(3-mercaptopropionate) via S-S bonding, and distributed throughout the cured cement. In the presence of a fracture, the polymer flows into the fracture interface strongly but reversibly anchoring through hydrogen bonding and ionic Ca−O bonds. In addition, it was found that the polymer S−S groups undergo reversible sulfur exchange. These polymer-cement and polymer-polymer reversible and dynamic interactions are responsible for the self-healing capability of this novel polymer-cement composite 1[11].

A number of reports on the effect of using polymers to increase adhesion to steel exist in the open literature [12-14]. For example, the addition of a different vinyl acrylic-based polymer to coat steel rebars have been studied as a way to increase cement-steel adhesive strength [13]. Other approaches introduce polymers directly in the cement slurry. For instance, it has been shown that polyacrylic esters, poly(vinylidene chloride-vinyl chloride), and chloroprene rubber (CR) latexes interact with Calcium ions and $Ca(OH)_2$ surfaces forming chemical bonds and increasing cohesive forces in the cement matrix and aiding to adhesive strength at cement-steel

interfaces [14]. The objective of this paper was to investigate adhesive bond strength and bond strength recovery to steel wellbore casing of two polymer-cement composites developed by this research group; the above described composite 1 and a second polymer-cement composite (composite 2). Composite 2, which is obtained by introducing 10wt% of Poly(ethylene-co-acrylic acid) zinc salt and 5wt% of equimolar quantities of Bisphenol A diglycidyl ether, N,N-Dimethylethylenediamine, poly(ethylene glycol) diglycidyl ether, and Ethylenediamine to conventional cement H, was designed to be applied in geothermal wellbores with temperatures of up to 300 °C. The first component, Poly(ethylene-co-acrylic acid) zinc salt, was chosen to provide reversible coordination bonds with Calcium in cement, similarly to what this group demonstrated between alkoxides and Calcium in Composite 1[11, 15]. The other four monomers, which include two amines and two epoxides will form a crosslinked polymer by amine-driven ring-opening of the epoxides. This second crosslinked polymer should enhance the adhesive strength to steel as previously reported. In essence, amines are known to chemisorb to metal surfaces as well as promote partial dissolution of the surface oxide and/or hydroxide metallic layer. Then, metallic ions diffuse through the polymer layer and react with amine groups to form an organo-metallic complex by coordination bonding [12]. The self-healing as well as adhesive properties to steel casing of the above described two composites were evaluated by means of shear bond strength (SBS) tests [9, 16] and permeability analysis[10]. In addition, similar tests were conducted after exposing the cement composite samples to relevant geothermal conditions demonstrating the potential of these fit-for-purpose cement composites for application in high temperature geothermal wellbores.

2 Methods

2.1 Materials

Class H cement was supplied by LaFarge from the Joppa Plant. Silica flour (200 mesh) was obtained courtesy of U.S. Silica and measured in cement using XRD and EDS in previous related published work to be quartz[10]. Silica flour is commonly added to wellbore class G or H cement as a pozzolanic material to increase mineral stability. Thioplast EPS 25 (EPS 25) (640 g/1 equivalent epoxide) was supplied by Akzo Nobel, and 4-dimethylaminopyridine (DMAP), poly(ethylene glycol) diglycidyl ether (PEO) (250 g/1 equivalent epoxide), pentaerythritol tetrakis(3-mercaptopropionate) (4SH), Poly(ethylene-co-acrylic acid) zinc salt powder (Zn-salt), Bisphenol A diglycidyl ether (BPA) purchased from Sigma-Aldrich, N,N-Dimethylethylenediamine (NND), Ethylenediamine (ED) were purchased from Sigma-Aldrich. All materials were used as received.

Base cement samples were synthesized by mixing the class H cement powder (157.5 g) and silica flour (67.5 g) in a 600 ml poly(propylene) beaker, then adding 85.5 g of DI H_2O and mixing to obtain a homogeneous cement slurry. Cement was mixed with a Caframo overhead mixer with a 2-inch blade 4x impeller for a total of 15 minutes.

Polymer-cement “composite 1” samples were synthesized following previous work by this group [10] by mixing the polymer precursors (8.4 g EPS 25, 8.4 g PEO, 5.7 g 4SH) in an Al pan, followed by adding the homogeneous organic solution to the cement slurry prepared as described above but using 112.5g of water instead of 85.5g. Samples were cured to a maximum temperature of 200 °C as described in the next two sections. This temperature was chosen since thermogravimetric analysis on the polymer shows a reduction in mass at about 260 °C potentially due to thermal degradation.

Polymer-cement “composite 2” samples were synthesized by mixing monomers (BPA 4.8 g, PEO 4.8 g, NND 1.5 g, ED 0.2 g) in an Al pan until homogeneous. Separately, Zn-salt

powder (22.5 g) was added to the cement dry mix (consisting in class H cement powder, 157.5 g; and silica flour, 67.5 g) and mixed with 85.5g of water to make the slurry. After the first 10 minutes of mixing the Zn-salt modified cement slurry, the mixture of BPA, PEO, NND, and ED monomers were added to the slurry to generate composite 2. This procedure was found to provide a homogeneous slurry with no phase separation as opposed to adding all polymer precursors at the same time. Samples were cured to a maximum temperature of 300 °C as described in the next two sections. This temperature was chosen since thermogravimetric analysis on the polymer shows a reduction in mass at about 380 °C also potentially due to thermal degradation.

2.2 Shear Bond Strength

Adhesion and re-adhesion were tested in triplicate using a confined method similar to previously performed tests[9, 16]. For this test two pipes were aligned with their sides parallel to each other in an end cap jig. The inner pipe, made from either 316 stainless steel or carbon steel, (12.7 mm diameter and 50.8 mm long) and outer (confining) pipe, made from 316 stainless steel, (38.1 mm diameter x 38.1 mm) are placed inside of the end cap, which was machined so that the top of the inner tube and outer tube sit on an equal level (Figure 1). Once the cement slurry was prepared it was poured into the annulus formed between the inner and outer pipes. After pouring the cement into the annulus, the system was tamped to free any trapped air. Using a trowel, excess cement was scraped off the top of the assembly. The samples were cured at room temperature for 24h in 100% relative humidity (RH), followed by a second curing period of 24h at 85 °C and 100% RH, and a third and final curing period of five days at 200 °C in a Parr reactor at 100% RH. Once the curing process was completed, the samples were carefully removed from the bottom end cap (Figure 1). Shear bond strength (SBS) testing was performed

by fabricating a test jig and using a test frame model MTS 50Kip in conjunction with Bluehill by Instron controls and data acquisition software. Samples were placed inside of the test jig with the inner pipe protrusion up. Force was applied at a rate of 1,800 lb/min, with the maximum load defined as the force required to cause the inner pipe to initially slip. Once the test was completed the sample was inverted and the inner steel pipe compressed back to its original position for the second "after heal" test. The samples were reacted a second time at 200 °C in a Parr reactor at 100% RH after which the adhesive bond strength was tested a second time. The shear bond strength is calculated following API Specifications 10A, using equation 1:

$$SBS = \frac{P}{A} \quad [1]$$

Where:

SBS = shear bond strength (MPa); *P* = maximum load (lbf); *A* = area of bonding surface (in^2)

2.3 Permeability tests

Saturated permeability was conducted to test the ability for the cement polymer composites to heal and reduce flow through aperture. These tests evaluated the changes that occur in cement fracture or in the micro-annulus between the cement and the casing. In this case the debonded micro-annulus aperture was evaluated as if it was equivalent to a fracture in the cement. All permeability tests were conducted in triplicate and were conducted in a similar fashion to previously published work on flow through fractured rock and cement[17, 18].

Cement-casing samples were prepared and cured as described in the previous section (2.2 Pipe-shear test). After curing, the cement was debonded from the pipe casing by pushing the

cement half-way out of the pipe three times. The cement was then reset to the original position for the permeability tests.

Cement fracture test samples were prepared by pouring cement slurry into tube molds creating monoliths with an average length of 4 cm and diameter of 2.5 cm. Similarly, to the cement-casing samples, the cement monoliths were initially cured at room temperature for 24h in 100% relative humidity (RH), followed by a second curing period of 24h at 85 °C and 100% RH, and a third and final curing period of five days at 200 °C (composite 1) and 300 °C (composite 2) in a PARR reactor at 100% RH. Cured samples were removed from molds and cut to length with a rock saw, and the sides bound with heavy-duty moisture-seal heat-shrink tubing after removing glue from the tubing. These monoliths were then placed upright in a hydraulic press. Tension in the center of the cylinder was applied until samples cracked across the length of the sample generating a longitudinal fracture.

Both fractured cement monoliths and cement-casing samples were fixed with end caps. Permeability was tested using the saturated constant head method [19] where constant head pressure was maintained by keeping the reservoir (sealed vessel) at a constant air pressure (10 kPa) and the discharge was measured at atmospheric pressure. Reynolds equation (Equation 2) [17] for flow through fractured (cylindrical cement monoliths) or debonded media (cement-casing samples) was arranged to solve for the effective fracture aperture (Equation 3). This aperture could be translated to a representative permeability by using the relationship in Equation 4:

$$Q = -\frac{Wb^3}{12\mu}\left(\frac{P_o - P_i}{l}\right) \quad [2]$$

$$b = \sqrt[3]{\frac{-12\mu Q}{W}\left(\frac{l}{P_0 - P_i}\right)}$$

192 [3]

193

194 k_i [4]
b^2

195

196 Where:

197 Q = discharge ($cm^3\ s^{-1}$); W = estimated fracture width for cement fracture test or pipe inner
198 circumference for cement casing interface test (cm); b = aperture (cm); μ = dynamic viscosity
199 (Pa·s); P_o = pressure from pump (Pa); Pi = pressure from atmosphere (Pa); l = length of sample
200 (cm); k_i = permeability.

201 Once initial permeability values were determined, the samples were cured (healed) again
202 at 200 ºC (composite 1) and 300 °C (composite 2) and 100% RH for 5 days in a Parr reactor. The
203 permeability of the samples after this second curing period were tested for a second time as
204 described above.

205 ***2.4 Exposure tests***

206 Similar cement-casing samples were prepared for pipe-shear testing as described to
207 evaluate the cement-steel adhesive strength after exposure to thermal and chemical stress
208 regimes representative of geothermal environments. Exposure tests included: 1) thermal shock,
209 2) CO_2 exposure, 3) H_2SO_4 exposure. Triplicate samples were fabricated for each exposure test.
210 For the chemical exposure tests (CO_2 and H_2SO_4) "imperfections" were engineered into the
211 cement using 0.5 mm stainless steel wires. The wires were positioned to generate 4 holes along
212 the length of the inner steel pipe-cement interface (Figure 2). Once the cement was set, the wires
213 were pulled from the cement leaving a void for gas and liquid to enter the full length of the

cement-steel interface. The cement and polymer-cement composite samples were cured at room temperature for 24h in 100% relative humidity (RH), followed by a second curing period of 24h at 85 °C and 100% RH, and a third and final curing period of five days at 200 °C for base cement and composite 1 and 300 °C for composite 2 in a Parr reactor at 100% RH.

Exposure tests were performed at the National Energy and Technology Laboratory in Albany, Oregon. For thermal shock tests, the samples were subject to six thermal shock cycles. Each cycle consisted in heating the samples to 250°C and maintaining this temperature for 24 hours followed by a 5-minute quenching period with milli Q water at 22°C followed immediately by the next heating cycle at 250°C for 24 hours. For CO_2 exposure tests, the cured cement and polymer-cement samples were immersed in 1 wt.% NaCl brine and pressurized with 20.7 MPa of supercritical CO_2 at 90°C for one week. With H_2SO_4 exposure tests, samples were kept at ambient pressure at 90°C and in a brine of 1wt.% NaCl with H_2SO_4 at pH = 2. For this test the fluid was replaced daily with 650 ml of pH=2 brine.

2.5 Tomography

Tomography of cement samples were conducted at both Environmental and Molecular Sciences Laboratory (EMSL; Richland WA) and at the SRX Beamline (Brookhaven NY). At EMSL a X-ray computed tomography (XCT), Nikon XTH 320/225 was used to obtain 3D volume data at up to 20-50 µm resolution on sections of cement cores (depending on specimen size), which can then be viewed as sliceable images on the computer and analyzed for structural and density changes. XCT images of each piece were collected at high resolution, so that each exposed and unexposed sample could be compared. The 3D data on the cement was then processed in ImageJ [ImageJ: Image Processing and Analysis in Java. Available from: http://imagej.nih.gov/ij/ (2017)] to enhance contrast. The density or structural changes were

emphasized with the WEKA segmentation tool in ImageJ/Fiji. The different colors of the segmentation classes' show were the treatment effects the samples.

2.6 Density functional modeling

A series of density functional calculations were performed to examine the bonding motifs of a cement/polymer/steel interface. The cement model was based on a form of calcium silicate hydrate (CSH). These authors adopted the CSH model used in our recent study[1, 16], while the steel surface was represented with hematite – an oxide form of iron, as used in the literature[20]. The (0001) surface of hematite with the Fe-termination (stoichiometric) was chosen since it is a stable structure in a normal atmospheric environment [21]. For the polymer, the method adopted was the one used in our previous work[11].

In our CSH and hematite slab models, hematite is made up with 4 layers (480 atoms) while CSH is made up with 678 atoms. The 2D unit cell is 3.04 x 1.75 nm^2. For the geometry of the polymer on a hematite surface, the 2D unit cell of this system is 1.52x1.75 nm^2, made up with 356 atoms (116 polymer atoms and 240 hematite atoms).

Spin-polarized density-functional theory calculations were used, with the antiferromagnetic phase of hematite[22]. The density-functional PBE[23], with the D3 correction[24], in the CP2K package[25], was employed. *Ab initio* molecular dynamics (AIMD) simulations were carried out at 300 K, within the NVT ensemble, the time step for equations of motion integration was set at 0.5 fs. Due to the exceedingly large supercell size of the hematite-steel interface, these authors just consider static geometry optimizations here. However, as shown below, information about the bonding picture at the interface can already be unveiled. For the polymer-steel systems, due to the flexibility of the polymer and the computationally affordable system size, a NVT MD run of 10 ps was carried out.

3 Results and Discussion

3.1 Adhesion bond and bond recovery

The initial adhesion bond of cement to steel was tested by using SBS measurements between cement and steel pipe (Figure 3). Stainless steel as well as carbon steel were used in the tests since both type of materials are used in wellbore casing. When comparing the SBS values between stainless steel and carbon steel, adhesion to carbon steel was higher than to stainless steel for base cement and for both cement composites. Furthermore, base cement showed the highest adhesive strength to both, carbon steel (15.8 MPa) and stainless steel (7.9 MPa). Of the two composite cements tested, composite 2 showed the highest adhesive strength to both stainless steel and carbon steel with values of 4.7 MPa and 9.2 MPa, respectively (Figure 3).

Recovery of adhesion was evaluated by determining the ratio of second SBS test (post-healing) to initial SBS. For stainless steel adhesion, base cement and composite 2 showed an adhesive strength recovery of 0.5 (50% of original SBS values). Composite 1 had an adhesion recovery ratio of 1.7 (the second adhesive strength value was higher than the initial value), but its average initial SBS was only 0.5 MPa. For carbon steel SBS the bond strength recovery of the composites was similar, 0.5 for composite 1 and 0.6 for composite 2. The highest SBS recovery was obtained with base cement to carbon steel which had a ratio of recovery of 0.7.

Cement adhesion to wellbore casing in a confined system is a function primarily of the different surface interactions cement and steel would develop over the lifetime of the wellbore. The adhesion may be also affected by the confining conditions where any expansion or contraction of the cement would change the contact surface at the cement-steel interface providing a change in spatial growth of crystalline structures with the resulting decrease or

increase in cement's SBS with the steel surface. Table 1 shows the change in dimensions of unconfined cylindrical samples of base cement and composites 1 and 2. The results on Table 1 show that, with exception of the length of composite 1 showing a reduction of -0.87% post-curing, in all cases the material undergo minimal shrinking post-curing (< 0.25 %).

During the curing process, the presence of water vapor in the 100% relative humidity environment and the CO_2 from air results in carbonation of cement along with corrosion of steel generating species such as $FeCO_3$ and $CaCO_3$ [6] forming a strong OFe covalent bond between casing and cement. These type of bonding is particularly expected between cement and carbon steel and seem to explain the significantly higher SBS values between cement and carbon steel (Base cement: 15.4 MPa, composite 1: 5.8 MPa, composite 2: 9.2 MPa; Figure 3b) as compared to the SBS values of cement and stainless steel (Base: 7.9 MPa, composite 1: 0.5 MPa, composite 2: 4.6 MPa; Figure 3a). In addition, the more reactive surface of the carbon steel generates additional surface area and surface roughness [26] which would contribute to higher cement-steel SBS. Though this would seem like a benefit and might suggest that carbon steel would make for a preferred wellbore material, corrosion of the casing is a very significant problem affecting the lifetime of wellbores in geothermal and fossil energy recovery. The fact that the polymer migrates to the steel surface (as it will be shown in Section 3.4) is advantageous since it could bring about corrosion-inhibiting properties to steel casing.

We have previously demonstrated that the presence of polymer in the cement matrix brings about autonomous healing to the composite due to the reversible and dynamic polymer-cement and polymer-polymer interactions[10, 11]. Furthermore, it was recently reported that the polymer acts as a temporary barrier for the hydration of cement aiding to the deployment/pumping of cement without the use of expensive retarders[27]. Therefore, a

contributing factor for the lower SBS values of the composite cements respect to base cement both cured for only five days could be associated to the following two phenomena; 1) the fact that the polymer acts as a retarder reducing the cement and cement-steel reaction (curing) rates, 2) the strength of the polymer-steel bonds (OFe, and SFe, and H bonds) described in the previous section may be lower than the OFe bond strength of base cement to steel.

When the cement-stainless steel samples were reacted for longer times, such as in the case of the thermally- and chemically-exposed samples (as it will be discussed in detail in Section 3.3), all the composites showed significantly higher values than their unexposed counterparts in agreement with the above hypothesis. Nevertheless, the reduction of adhesive strength during short curing times in composite materials can be mitigated reducing the concentration of polymer. For example, a recent study found that when the polymer concentration is equal or lower than 0.4 wt.% the compressive strength and SBS is similar to unmodified cement[22]. However, such lower concentrations of polymer will not produce ductile and self-healing materials, of critical importance for wellbore and other applications. A more detailed discussion of material's performance after thermal and chemical stress is described in Section 3.3.

3.2 Permeability Analysis

To evaluate the ability of cement and cement composites for autonomous self-healing, permeability tests were conducted through cement fractures or through a micro-annulus (channel created from deboning of cement from casing) before and after a five-day reaction/curing period at temperature (Figure 4). For fractured cement, where apertures averaged 85 µm (range 63-100

µm), there was a significant reduction in permeability post-healing of composite 1 with a resultant reduction of 70% of the original fracture's permeability (Figure 4a). Composite 2 also seems to show a decrease in fracture permeability post-healing. However, the permeability values are not statistically different to those of base cement (Figure 4a).

Permeability through the micro-annulus (cement-steel casing interface) yielded a different result where composite 2 had a significant reduction, over 50% after a healing event. Base cement showed no healing capability and an actual an increased in permeability post healing (Figure 4b). Composite 1 did not show signs of fracture healing at the steel interface like composite 2 did but there was significant scatter in the data with the possibility of some indication of healing in one of the samples. The aperture of the micro-annulus was calculated as average 10 µm (range 4-24 µm). Figure 4 also shows that base cement does not exhibit autonomous healing at either bulk cement or cement-steel interface.

As has been reported in our previous work[10, 28], in the presence of a fracture nearby polymers imbedded in the cement matrix will debond, transport into the fracture, and bond back sealing the fracture. This self-healing process that could occur multiple times throughout the lifetime of the composite is associated to the dynamic and reversible polymer-cement and polymer-polymer interactions that occur at temperature[10, 11]. The polymers in the cement are readily available to flow into interfaces due to their homogeneous distribution throughout the cement matrix as can be seen by the XCT mapping of polymer aggregates discussed in Section 3.4. Since polymer moieties are also present at the composite-steel interface and that similar reversible composite-steel bonding at the interface were unveiled by atomistic simulations (see discussion in next section), all seems to indicate that these composite materials could seal cement-steel gaps.

The aperture of the fracture as well as the concentration and mobility at temperature of the polymer may all play a role in the extent at which a bulk fracture or (cement-steel) interfacial gap is sealed. The aperture can be estimated using the Reynolds equation [Eqn 2]. In this study the fracture apertures averaged 85 µm in the bulk cement matrix (Figure 4a) and averaged 10 µm at the steel-cement interface (Figure 4b). The temperature-dependent mobility of the polymers in the cement matrix is associated, among other properties, to their molecular mass and degree of crosslinking, which is difficult to estimate in the polymer-cement composite. However, from the self-healing capability of composite 2 at the steel-cement interface, one could hypothesize that Zn salt polymer has a higher mobility (hence a lower molecular mass) than the highly crosslinked EPS25[10]. However, this is ruled out by the fact that Composite 1 outperforms Composite 2 when self-healing bulk cement fractures (Figure 4a). Then, the fact that Composite 2 outperforms Composite 1 for self-readhering (healing) at the interface cement-steel seems to be due to the presence of a second polymer system, in addition to the Zn salt polymer. This second polymer system obtained by the reaction of two amine monomers NND and ED with two epoxides BPA and PEO contains amine and hydroxyls functionalities known to enhance adhesive strength to steel via chemisorption to metal surfaces as well as the formation of organo-metallic complexes by coordination bonding[12]. These authors hypothesize that this is the main reason why Composite 2 outperforms Composite 1 in self-readhesion to steel casing with the corresponding larger reduction in permeability at the steel-cement interface.

3.3 Adhesion strength after exposure to thermal and chemical stresses

To examine how cement's adhesion to steel casing responds under thermal and chemical stresses typical of geothermal environments, exposure tests simulating thermal shock and chemical exposure were performed (Figure 5).

3.3.1 Thermal shock

The repeated heating and rapid cooling from thermal shock resulted on cement-steel samples resulted in an average SBS of 0.87 MPa for base cement and 4.67 MPa for composite 2 (Figure 5a). The reduction of initial SBS for base cement was significant after six thermal shock cycles compared to the equivalent non-exposed base cement sample (Figure 5a). After a curing/healing process the recovery of SBS yielded a significant increase for thermal shocked base cement (5.84 MPa). However, it is important to mention that the variability of SBS values post-healing was significant, demonstrating that base cement is highly vulnerable to thermal shock cycling (Figure 5a). Moreover, thermal shock of base cement generated radial fractures (Figure 6a). In the case of composite 2, the material not only showed high adhesive strength to stainless steel after six thermal shock cycles, but also demonstrated substantial re-adhesion (healing) capability with a recovery of SBS of over 150% (Figure 5a). Furthermore, composite 2 did not show evidence of radial fractures after thermal shock cycles (Figure 6b) demonstrating the positive impact that the polymer has, not only in bringing about re-adhesion to steel casing, but also in maintaining intact the integrity of the cement matrix.

Polymer addition to the cement then seems to maintain the original cement-steel adhesive strength and also buffer against the formation of radial fractures commonly found in geothermal and unconventional oil/gas wellbores. This ability to absorb the strain of the thermal shock could be due to the increased ductility of the polymer-modified cement material[28]. After the healing

(re-adhesion) reaction, the adhesive strength (SBS values) of base cement and composite 2 was restored and even increased compared to the original value. However, SBS values for base cement showed high variability. For the base cement new OFe covalent bonds would have been formed, perhaps from calcite formation. The 150% increase in SBS by composite 2 could be due to a combination of the cement-steel OFe bonds along with the covalent bonds between polymer O and hematite Fe pairs (OFe), polymer S and hematite Fe pairs (SFe), and H-bonds between the (O)H atoms of the polymer and hematite O pair as it will be discussed in Section 3.5.

3.3.2 Chemical exposure

Samples of base cement and composite 2 were also exposed to chemical stresses. Chemical exposure to H_2SO_4 and CO_2 seems to promote an increase in cement-stainless steel SBS for both, base cement and composite 2 as compared to SBS values obtained from unexposed samples (Figure 5b and 5c). This was particularly evident for samples exposed to CO_2 where the value of SBS was three times higher than the unexposed cement-steel samples (Figure 3a and 5b). In addition, base cement and composite 2 have statistically similar SBS values post-CO_2 exposure. When it comes to re-adhesion (healing) the cement-stainless steel interfacial bond, it was observed a statistically similar and partial recovery of the SBS for both, base cement and composite 2 (Figure 5b and 5c). It is worth noting, anecdotally, that both thermal shock and CO_2 exposure base cement samples were quite brittle and crumbled when tests were dismantled, whereas all H_2SO_4 samples and thermal shock and CO_2 composite 2 remained intact.

The exposure to CO_2 has been reported to alter the elemental distribution of both base cement and polymer-cement composite[29] and lead to the creation of three distinct zones with calcite formation and dissolution throughout the reaction zones, as consistent with those

415 described in Kutchko, Strazisar, Dzombak, Lowry and Thaulow [30]. Gil et al[29] showed that
416 these carbonation reactions were particularly evident in base cement and that the presence of the
417 polymer in the composite partially buffers the carbonation reaction. The increase of SBS in base
418 cement after CO_2 exposure could be due to the formation of calcite at the interface as previously
419 reported. The growth of calcite crystals would likely increase the number of OFe bonds at the
420 steel interface, The increase in SBS on the composite 2-steel samples could be the result of both,
421 longer curing times (like in the case of thermal shock exposure) and, to a lesser extent, calcite
422 formation. Re-adhesion (healing) was statistically similar for base cement and composite 2 and
423 below 50% recovery for both materials. It is important to mention that, although the composite-
424 steel bonds may not be as strong as base cement-steel bonds, it is clear that polymer migrates to
425 the steel-cement interface sealing gaps as demonstrated by the permeability analysis discussed in
426 the next section.

427 As in the case of CO_2-brine exposure, the values of SBS significantly increased for both,
428 base and composite cements, after exposure to H_2SO_4 in brine. In this case, the formation of
429 gypsum is expected to take place from the reaction of H_2SO_4 with $Ca(OH)_2$ as previously
430 reported. Ettringite is also a product formed from the continuous reaction of sulfuric acid with
431 cement[31]. Gypsum and ettringite are mechanically strong (and may be the reason why the
432 adhesive strength increases in both materials. Although stainless steel is corrosion resistant, a
433 combination of sulfuric acid pH=2 with brine is highly corrosive, particularly at high
434 temperatures (90 °C in our study). However, the slow dissolution rates (~0.1mm/year) for
435 stainless steel under these conditions would play an insignificant role given the fact that chemical
436 exposure only lasted 7 days[32]. Nevertheless, in wellbore applications where the average
437 lifetime is 30 years, corrosion of the casing is an important issue and cement-steel adhesion plays

a critical role in preventing fluids flow into the interface and the associated corrosion of the casing. As in the case of post-exposure SBS, post-healed adhesive strength at the interface was statistically similar between base cement and composite 2. In both material the adhesion recovery after mechanically-induced debonding was below 50% after 5-day healing reaction. Once again, the migration of polymer to the cement-steel interface evidenced in Figure 7 would play a critical role in preventing the formation of fluid pathways.

In summary, all H_2SO_4-brine exposed samples showed no significant change in adhesive strength as compared to the as-prepared materials. On the other hand, base cement samples were quite brittle and crumbled when tests were dismantled after exposure to both thermal shock and CO_2-brine. In contrast, composite 2 exposed to thermal shock and CO_2 remained intact, once again demonstrating the significant benefit that the polymer brings about to the cement matrix in terms of structural integrity as well as self-healing and re-adhering capability.

3.4 Tomography

Tomography was used to investigate the presence and distribution of polymer throughout the cement composite matrix as well as to determine the material's porosity (Figure 7, Table 2). Grey scale XCT images show no difference among low density components, such as polymer and air (Figure 7, top row). However, with use of Image J software, density contrast can be enhanced enabling the production of the images shown in the bottom row of Figure 7. These false color images correspond to as synthesized base cement and polymer-cement composites 1 and 2 used for adhesion tests (Figure 7). From these false color images, air-filled pore volume and polymer volume was calculated (Table 2).

As expected, the images show no trace of polymers in the base cement sample (Figure 7a), while in the polymer-cement composites, the polymer is distributed throughout the matrix of the cement (Figure 7b and 7c). The polymers appear to aggregate in distributed pockets. These aggregations generally account for most of the polymer added with composite 1 having 7.7 vol% of polymer (10 wt% polymer is originally added), and composite 2 having 13.3 vol% of polymer when 15 wt% polymer was originally added (Table 2). From the color images it can also be seen that the polymer for both composite 1 and composite 2 can be found in the interface between cement and casing. This can be seen on the curved sections of the samples where the cement had previously been in contact with the inner and outer pipes (Figure 7 b and c, bottom row). The cement was removed from the annulus of the pipes before imaging.

3.5 Density functional modeling of steel/cement and steel/polymer interfaces

Atomistic simulations of the steel/cement and steel/polymer interfaces were conducted to obtain information about atomic interactions and types of bonding. In Figure 8(a), it is shown a relaxed atomic structure at the CSH/hematite interface, which are used to model the cement/steel interface. There is significant atomic re-arrangement at the interface indicating strong interactions, between Ca atoms of CSH and O atoms of hematite, as well as O of CSH and Fe of hematite. These interactions are depicted by the computed radial pair distribution functions in Fig. 9(b). In fact, the OFe pair g(r) shows that there are OFe covalent bonds between CSH and hematite.

The peak position at about 2 Å is similar to FeO bond lengths of the hematite. For the CaO pairs, it was found a peak at about 2.5 Å, which is slightly larger than CaO distances in CSH, (about 2.3 Å). It is not surprising that the smallest distance between cations Ca^{2+} and Fe^{3+}

481 at the interface is about 2.9 Å, which is considerably larger than the sum of their ionic radii of ~
482 1.9 Å.

483 In a second simulation, these authors examined the interactions between polymer and
484 hematite, shown in Figure 9(a). During the simulation time of 10 ps, the polymer is shown to
485 relax and wet the hematite surface, see Fig. 9(b). Considering the atomic density along the z
486 direction normal to the hematite surface, the high-density double peak extending to about 5 Å
487 from the hematite surface, is indicative of strong adhesion of the polymer to the surface. To
488 understand the bonding motif between the polymer and the hematite surface, the radial pair
489 distribution function was also calculated, Fig. 9(c). A sharp peak at 2.1 Å indicates covalent
490 bonds between polymer O and hematite Fe pairs. Similarly, the peak at 2.5 Å between polymer S
491 and hematite Fe pairs also indicates covalent character, albeit a weaker one. Finally, it was also
492 observed weak H-bonds between the (O)H atoms of the polymer and hematite O pair, at about
493 2.2 Å, implying that hydrogen bonding between the polymer and the hematite surface also
494 stabilize this interaction.

495 In summary, base (unmodified) cement-steel interaction takes place via two main bond
496 motifs, OFe (O of cement and Fe of hematite) and CaO (calcium of cement and Oxygen of
497 hematite) while in the polymer-cement composite the polymer brings about three additional
498 polymer-hematite interactions with the stronger one being OFe (oxygen of the polymer with iron
499 of the hematite). This particular polymer-hematite bonds seems to be stronger than cement-
500 hematite bonds, based on bond distance. However, based on the SBS results previously discussed
501 where cement-steel adhesive strength is higher for both stainless steel and carbon steel compared
502 to composite-steel values, additional interactions may play a role in the adhesive properties of

these materials. Nevertheless, atomistic simulations represent a powerful tool to design and predict macroscopic properties of advanced cement materials.

5 Conclusion

Debonding of wellbore cement at the casing-cement interface results in leakage pathways with the potential for unwanted fluid migration. Adhesion was proven to be stronger for cement-carbon steel as compared to cement-stainless steel and is hypothesized to be due to the higher reactive nature of the carbon steel in extreme/corrosive (high RH and temperature) environments. Atomistic simulations show the formation of OFe bonds between cement and steel and OFe, SFe, and H-bonds between polymer and steel in the cement composite materials. The simulations indicate that the presence of polymer introduces bonding interactions with the casing at distances where there are fewer/weaker interactions with the cement. Adhesion to stainless steel after exposure to thermal shock shows to be weaker in the case of base cement as compared to polymer-cement composite 2. However, polymer-cement composite 2 shows a consistent recovery (150% of the original) of adhesive strength post-healing as compared to base cement . Cement-stainless steel adhesion post-exposure to CO_2/brine and mineral acid/brine was statistically similar for base cement and composite 2. The recovery of adhesive strength (re-adhesion) after debonding and healing was statistically similar for both base cement and composite 2.

Permeability studies before and after curing a longitudinal fracture showed that composite 1 exhibits self-healing capability with a reduction in permeability of 70% post-healing. Re-adhering capability to stainless steel casing was also studied by micro-anulus permeability analysis before and after curing a debonded cement-steel interface. The results

showed that composite 2 exhibits an average reduction in permeability of over 50% post-healing. Base cement does not exhibit autonomous healing at either bulk cement or cement-steel interface based on permeability analysis. In summary, these novel polymer-cement composites bring about self-healing and re-adhering (to steel casing) properties compared to conventional wellbore cement. This was particularly evidenced by the filling of fractures and interstitial gaps as demonstrated by tomography and permeability results.

Acknowledgements

Funding provided by the Department of Energy's Geothermal Technology Office. PNNL is operated by Battelle for the U.S. DOE under Contract DE-AC06-76RLO 1830. Part of this research was performed at the W.R. Wiley Environmental Molecular Sciences Laboratory (EMSL), a national scientific user facility at PNNL managed by the Department of Energy's Office of Biological and Environmental Research, and simulations were performed with resources from PNNL's Research Computing and the National Energy Research Scientific Computing Center, a DOE Office of Science User Facility supported by the Office of Science of the U.S. Department of Energy under Contract No. DE-AC02-05CH11231. Kenton Rod and Carlos A. Fernandez contributed equally to this manuscript.

References

[1] E.B. Nelson, D. Guillot, Eds., Well Cementing, 2nd ed., Schlumberger, Sugar Land, TX, 2006.

[2] R. Shortall, B. Davidsdottir, G. Axelsson, Geothermal energy for sustainable development: A review of sustainability impacts and assessment frameworks, Renew. Sust. Energ. Rev., 44 (2015) 391-406.

[3] R.J. Davies, S. Almond, R.S. Ward, R.B. Jackson, C. Adams, F. Worrall, L.G. Herringshaw, J.G. Gluyas, M.A. Whitehead, Oil and gas wells and their integrity: Implications for shale and unconventional resource exploitation, Marine and Petroleum Geology, 56 (2014) 239-254.

[4] R. Kiran, C. Teodoriu, Y. Dadmohammadi, R. Nygaard, D. Wood, M. Mokhtari, S. Salehi, Identification and evaluation of well integrity and causes of failure of well integrity barriers (A review), Journal of Natural Gas Science and Engineering, 45 (2017) 511-526.

[5] J.W. Carey, M. Wigand, S.J. Chipera, G. WoldeGabriel, R. Pawar, P.C. Lichtner, S.C. Wehner, M.A. Raines, G.D. Guthrie, Jr., Analysis and performance of oil well cement with 30 years Of $CO_{(2)}$ exposure from the SACROC Unit, West Texas, USA, International Journal of Greenhouse Gas Control, 1 (2007) 75-85.

[6] J.W. Carey, R. Svec, R. Grigg, J. Zhang, W. Crow, Experimental investigation of wellbore integrity and CO2-brine flow along the casing-cement microannulus, International Journal of Greenhouse Gas Control, 4 (2010) 272-282.

[7] E. Therond, A.-P. Bois, K. Whaley, R. Murillo, Large-Scale Testing and Modeling for Cement Zonal Isolation in Water-Injection Wells, Spe Drilling & Completion, 32 (2017) 290-300.

[8] Z. Luo, S. Bryant, Influence of thermo-elastic stress on fracture initiation during CO2 injection and storage, Energy Procedia, 4 (2011) 3714-3721.

[9] R.B. Carpenter, J.L. Brady, C.G. Blount, EFFECTS OF TEMPERATURE AND CEMENT ADMIXES ON BOND STRENGTH, Journal of Petroleum Technology, 44 (1992) 880-&.

[10] M.I. Childers, M.T. Nguyen, K.A. Rod, P.K. Koech, W. Um, J. Chun, V.A. Glezakou, D. Linn, T.J. Roosendaal, T.W. Wietsma, N.J. Huerta, B.G. Kutchko, C.A. Fernandez, Polymer-Cement Composites with Self-Healing Ability for Geothermal and Fossil Energy Applications, Chem. Mat., 29 (2017) 4708-4718.

[11] M.T. Nguyen, Z.M. Wang, K.A. Rod, M.I. Childers, C. Fernandez, P.K. Koech, W.D. Bennett, R. Rousseau, V.A. Glezakou, Atomic Origins of the Self-Healing Function in Cement-Polymer. Composites, Acs Applied Materials & Interfaces, 10 (2018) 3011-3019.

[12] J. Bouchet, A.A. Roche, The formation of epoxy/metal interphases: Mechanisms and their role in practical adhesion, Journal of Adhesion, 78 (2002) 799-830.

[13] J.J. Assaad, C.A. Issa, Effect of Recycled Acrylic-Based Polymers on Bond Stress-Slip Behavior in Reinforced Concrete Structures, Journal of Materials in Civil Engineering, 29 (2017).

[14] Y. Ohama, Handbook of Polymer-Modified Concrete and Mortars, Properties and Process Technology, 1st ed., William Andrew1995.

[15] M.-T. Nguyen, Z. Wang, K.A. Rod, M.I. Childers, C. Fernandez, P.K. Koech, W.D. Bennett, R. Rousseau, V.-A. Glezakou, Atomic Origins of the Self-Healing Function in Cement–Polymer Composites, ACS Applied Materials & Interfaces, 10 (2018) 3011-3019.

[16] X.F. Zhao, Z.C. Guan, M.L. Xu, Y.C. Shi, H.L. Liao, J. Sun, The Influence of Casing-Sand Adhesion on Cementing Bond Strength, Plos One, 10 (2015).

[17] M.J. Nicholl, H. Rajaram, R.J. Glass, R. Detwiler, Saturated flow in a single fracture: Evaluation of the Reynolds equation in measured aperture fields, Water Resour. Res., 35 (1999) 3361-3373.

[18] K.A. Rod, W. Um, S.M. Colby, M.L. Rockhold, C.E. Strickland, S. Han, A.P. Kuprat, Relative permeability for water and gas through fractures in cement, Plos One, 14 (2019).

[19] A. Klute, C. Dirksen, Hydraulic Conductivity and Diffusivity: Laboratory Methods, in: A. Klute (Ed.) Methods of Soil Analysis, Part 1 - Physical and Mineralogical Methods, American Society of Agronomy, Inc, Soil Science Society of America, Inc,, Madison, WI, 1986, pp. 687-734.
[20] R. Olsen, K.N. Leirvik, B. Kvamme, T. Kuznetsova, Effects of Sodium Chloride on Acidic Nanoscale Pores Between Steel and Cement, The Journal of Physical Chemistry C, 120 (2016) 29264-29271.
[21] M.-T. Nguyen, N. Seriani, R. Gebauer, Water adsorption and dissociation on α-Fe2O3(0001): PBE+U calculations, The Journal of Chemical Physics, 138 (2013) 194709.
[22] J.J. Assaad, Development and use of polymer-modified cement for adhesive and repair applications, Construction and Building Materials, 163 (2018) 139-148.
[23] J.P. Perdew, K. Burke, M. Ernzerhof, Generalized Gradient Approximation Made Simple, Physical Review Letters, 77 (1996) 3865-3868.
[24] S. Grimme, J. Antony, S. Ehrlich, H. Krieg, A consistent and accurate ab initio parametrization of density functional dispersion correction (DFT-D) for the 94 elements H-Pu, The Journal of Chemical Physics, 132 (2010) 154104.
[25] J. VandeVondele, M. Krack, F. Mohamed, M. Parrinello, T. Chassaing, J. Hutter, Quickstep: Fast and accurate density functional calculations using a mixed Gaussian and plane waves approach, Computer Physics Communications, 167 (2005) 103-128.
[26] G. Chilkoor, N. Shrestha, D. Soeder, V. Gadhamshetty, Corrosion and environmental impacts during the flowback water disposal associated with the Bakken shale, Corrosion Science, 133 (2018) 48-60.
[27] M. Zysset, D. Berggren, Retention and release of dissolved organic matter in Podzol B horizons, European Journal of Soil Science, 52 (2001) 409-421.
[28] K.A. Rod, M.T. Nguyen, M. Elbakhshwan, S. Gills, B. Kutchko, T. Varga, A.M. McKinney, T.J. Roosendaal, M.I. Childers, C.H. Zhao, Y.C.K. Chen-Wiegart, J. Thieme, P.K. Koech, W. Um, J. Chun, R. Rousseau, V.A. Glezakou, C.A. Fernandez, Insights into the physical and chemical properties of a cement-polymer composite developed for geothermal wellbore applications, Cement & Concrete Composites, 97 (2019) 279-287.
[29] M.S. Elbakhshwan, S.K. Gill, K.A. Rod, E. Bingham, N.J. Huerta, C.L. Lopano, B.G. Kutchko, Y.K. Chen-Wiegart, C. Zhao, G. Williams, J. Thieme, T. Varga, L.E. Ecker, C.A. Fernandez, Structural and chemical changes from CO2 exposure to self-healing polymer cement composites for geothermal wellbores, (submitted in review).
[30] B.G. Kutchko, B.R. Strazisar, D.A. Dzombak, G.V. Lowry, N. Thaulow, Degradation of well cement by CO_2 under geologic sequestration conditions, Environ. Sci. Technol., 41 (2007) 4787-4792.
[31] A.M. Izzat, A.M.M. Al Bakri, H. Kamarudin, A.V. Sandu, G.C.M. Ruzaidi, M.T.M. Faheem, L.M. Moga, Sulfuric Acid Attack on Ordinary Portland Cement and Geopolymer Material, Revista De Chimie, 64 (2013) 1011-1014.
[32] BSSA, Selection of stainless steels for handling sulphuric acid (H_2SO_4), in: B.S.S. Association (Ed.), British Stainless Steel Association, Sheffield, UK, 2018.

Tables and Figures

Table 1. Average % of change in dimensions (diameter and length) of cylindrical cement monoliths for base cement, composite 1, and composite 2.

Sample	Average length change (% of total)	Average diameter change (% of total)
Base	-0.13%	-0.22%
Composite 1	-0.87%	0.01%
Composite 2	0.07%	-0.02%

Table 2. Porosities calculated from 3D XCT images for base cement, composite 1, and composite 2.

Sample	Volume air void (% of total)	Volume polymer (% of total)
Base	0.06	No polymer
Composite 1	0.24	7.70
Composite 2	1.4	13.3

634 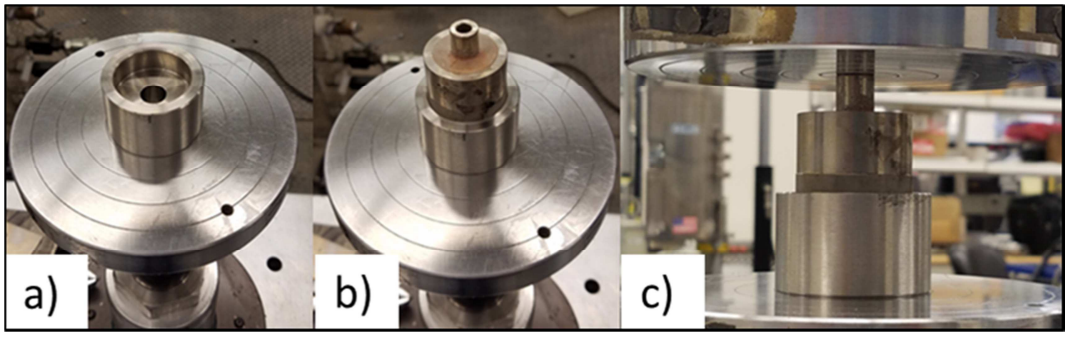

635 **Figure 1.** Set up for pipe-shear test: a) test base jig, b) confined cement-pipe system on top of
636 base (note cement composite is in annulus between pipes), c) pipe shear test being performed in
637 hydraulic press.

638

639

640 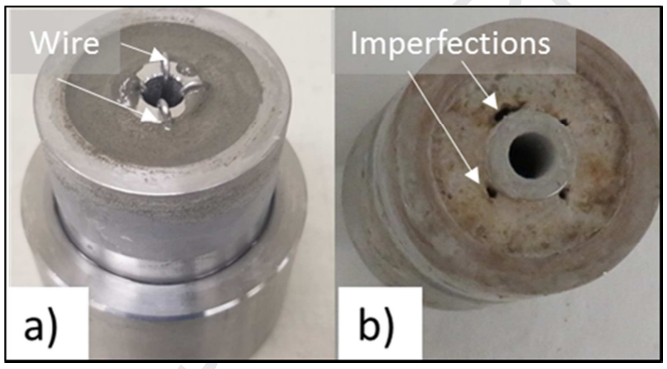

641 **Figure 2.** Pipe shear samples with "imperfections" engineered into samples. a) "Imperfections"
642 were from 0.5 mm stainless steel wire hung at 4 equally spaced positions along the 1.27 cm
643 diameter inner pipe before poring cement slurry. b) Wire was removed after cement was set
644 leaving holes that ran the length of the cement pipe interface.

645

646

647

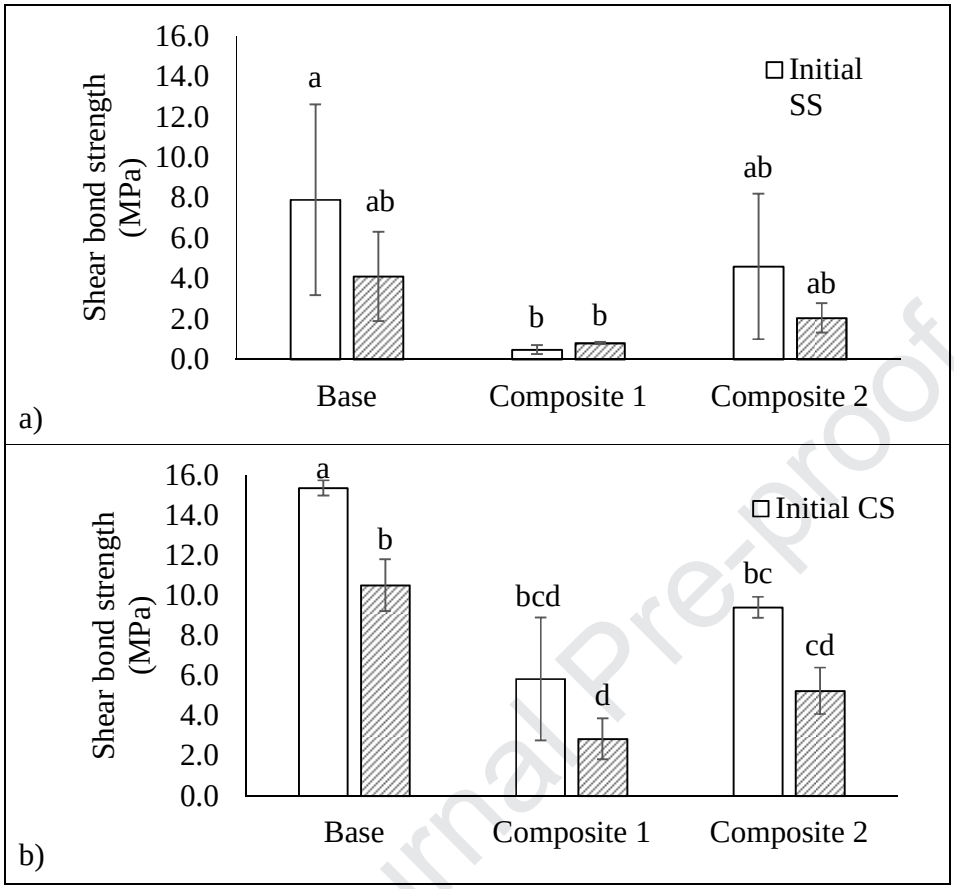

Figure 3. Shear bond strength for base cement, composite 1 and composite 2 for initial conditions and after healing for: a) 316 stainless steel, and b) carbon steel. Error bars represent one standard deviation calculated from triplicate samples. Letters not shared on graph (above bars) are significantly different via multiple-comparison Fisher's method.

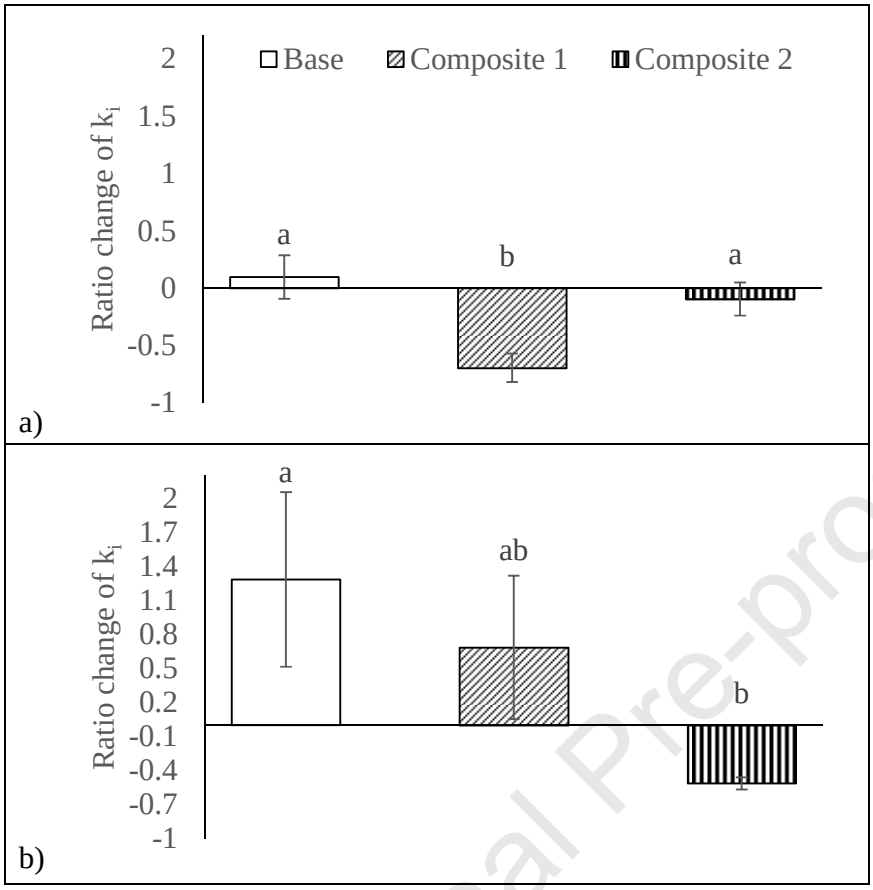

654 **Figure 4.** Ratio change of permeability (k_i) comparing before and after 5-day reaction at 200C
655 for base cement, composite 1, and composite 2: a) fractured cement permeability; b)
656 permeability at interface of cement composite and 316 stainless steel after bond was broken.
657 Negative values signify a reduction in permeability post-healing. Error bars represent one
658 standard deviation calculated from triplicate samples. Letters not shared on graph (above bars)
659 are significantly different via multiple-comparison Fisher's method.

660

661

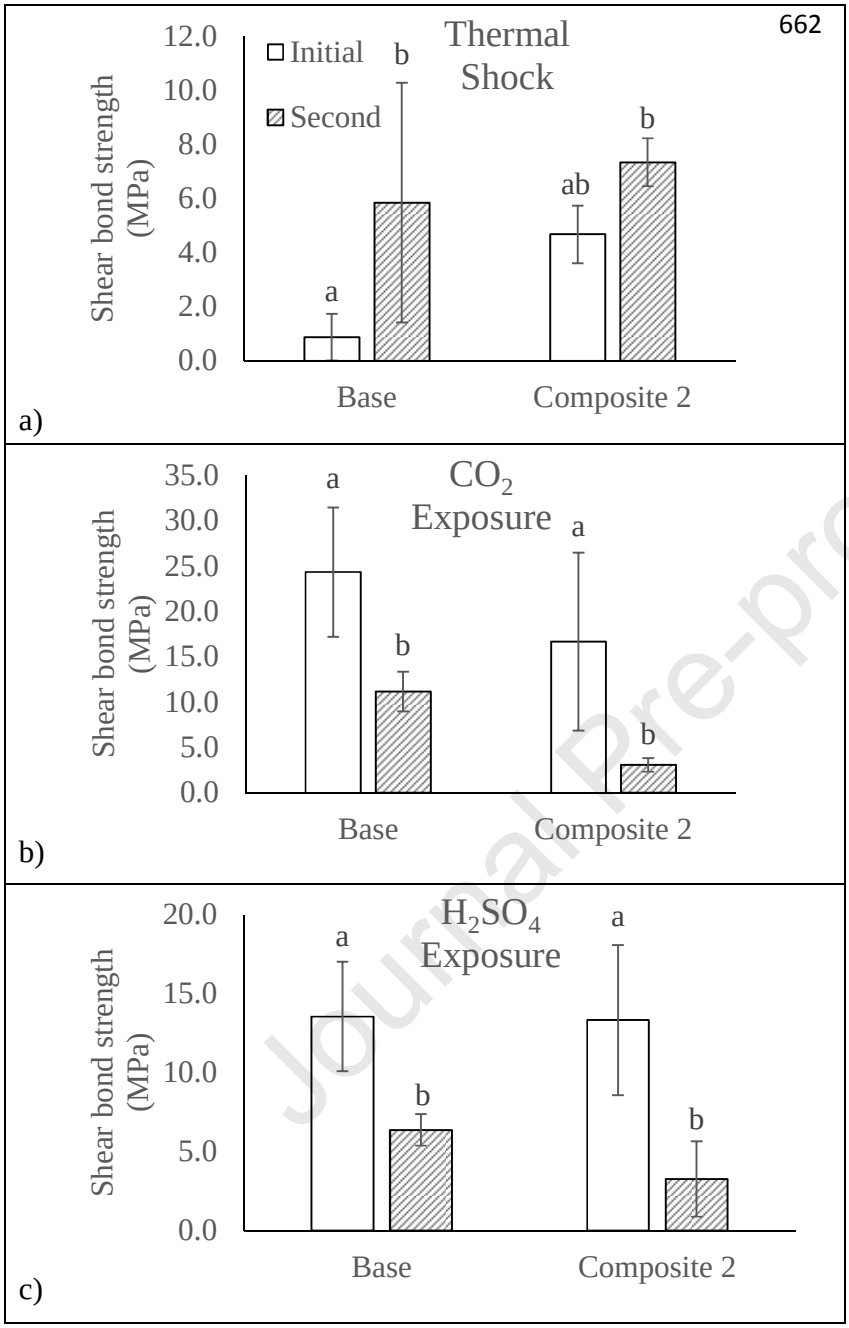

663 **Figure 5**. Shear bond strength for base cement and composite 2 to 316 stainless steel pipe after
664 exposure to representative geothermal conditions (initial condition) and after a second reaction
665 (healing) period for: a) thermal shock, b) CO_2 exposure, and c) H_2SO_4 exposure. Error bars
666 represent one standard deviation calculated from triplicate samples. Letters not shared on graph
667 (above bars) are significantly different via multiple-comparison Fisher's method.

668

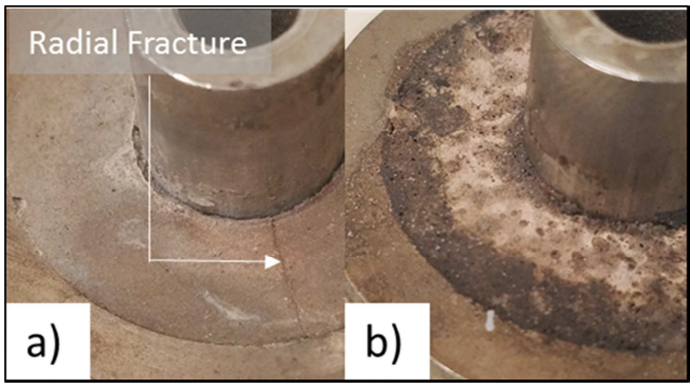

669

670 **Figure 6.** Image of cement adhesion samples after thermal shock where: a) base cement shows
671 radial fracture and b) cement composite 2 had no noticeable radial fractures. Dark staining on
672 cement composite 2 is polymer mobilized during reaction, which is responsible for self-healing
673 and re-adhering capability.

674

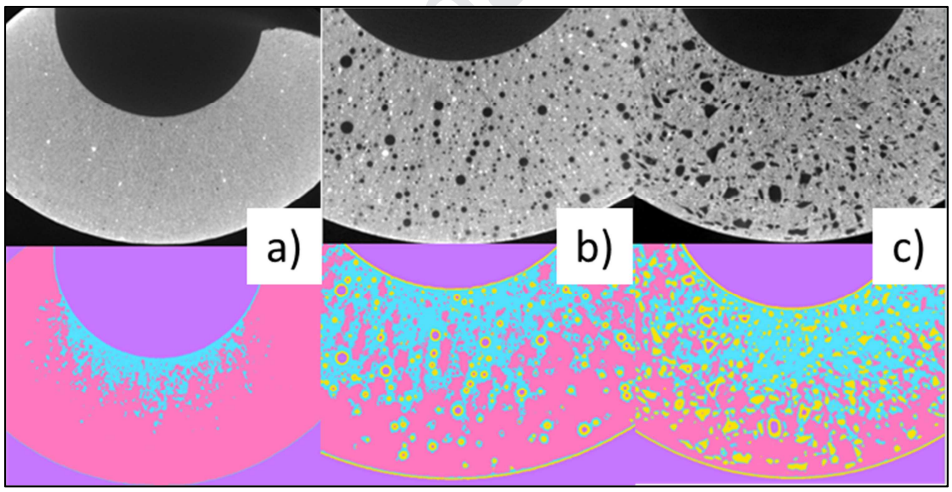

675

676 **Figure 7**. 2D XCT images of as-prepared cement samples from pipe shear experiments with
677 stainless steel pipes: a) base cement; b) composite 1; c) composite 2. Top row images are XCT
678 grey scale images, paired images on bottom row are false color classification of XCT. Grey scale

679 images: black = air and polymer, grey = cement, white = silicate minerals. Color images: purple
680 = air, yellow = polymer, blue = cement, pink = higher density cement.

681

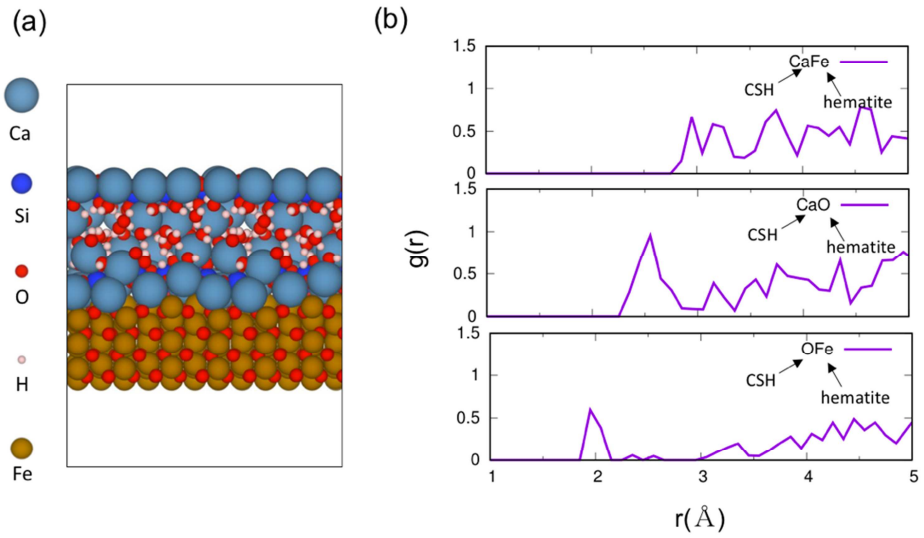

682

683 **Figure 8**. (a) Relaxed CSH-hematite interface, and (b) radial pair distribution function between
684 atoms of CSH (Ca, O) and that of hematite (Fe, O) right at the interface.

685

686

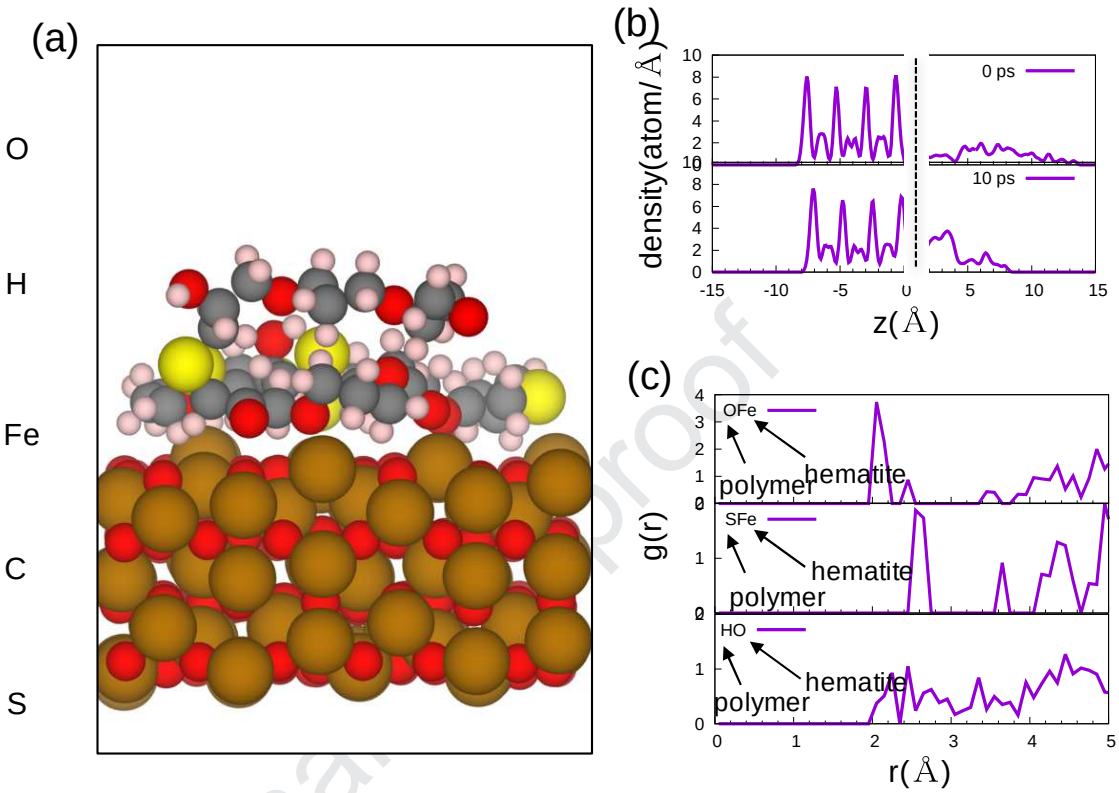

687

688 **Figure 9**. (a) Polymer/hematite structure at 10 ps of the AIMD simulation, (b) atomic density
689 along the z direction of the polymer/hematite system at 0 and 10 ps of the AIMD simulation, (c)
690 radial pair distribution function between atoms O, S, and H of CSH and Fe, Fe, and O of
691 hematite, respectively.

692

Polymer-cement composites with adhesion and re-adhesion (healing) to casing capability for geothermal wellbore applications

Kenton A. Rod[1#], Carlos A. Fernandez[1 # +], Manh-Thuong Nguyen[2], James B. Gardiner, Nicolas J. Huerta[4], Vassiliki-Alexandra Glezakou[2], Tamas Varga[5], Roger Rousseau[2], Phillip K. Koech[1]

No conflicts of interest in this submission.